Enhanced visible light photocatalytic activity of P-block elements (C, N and F) doped porous TiO$_2$ coatings on Cp-Ti by micro-arc oxidation

S. Sridhar · A. Viswanathan · K. Venkateswarlu ·
N. Rameshbabu · N. L. Parthasarathi

Abstract P-block elements (C, N and F) doped porous TiO$_2$ coatings were developed on commercially pure titanium by micro-arc oxidation (MAO) for visible light photocatalytic activity. Porous structured photocatalytic system has been developed with the use of different electrolytes. The geometry of porous coatings was analyzed by optical profilometer and their results confirmed that the surface roughness, width and depth of pores vary with respect to the doped elements. The anatase and rutile phase percentage in the pure and doped TiO$_2$ coatings was estimated by their XRD patterns. EDS analysis confirms the presence of C, N and F (2.2, 3.1 and 3.8 at.%) doped elements in the TiO$_2$ coatings. The band gap energies of C, N and F doped TiO$_2$ coatings were significantly reduced into 3.03, 3.04 and 3.02 eV, respectively than pure TiO$_2$ (3.15 eV) coating. The photoluminescence study indicates the formation of additional electronic states by the influence of C, N and F doped elements in TiO$_2$. This resulted in the reduced rate of recombination of photogenerated electron–hole pairs. The photocatalytic activity of MAO produced pure and doped TiO$_2$ coatings have been investigated with methylene blue dye as a target pollutant. The results confirmed that the doped TiO$_2$ showed higher rate of dye degradation than pure TiO$_2$. In particular F doped TiO$_2$ revealed higher photocatalytic activity among all other doped TiO$_2$.

Keywords Micro-arc oxidation · Porous coatings · P-block elements doped TiO$_2$ · Photocatalytic activity · Electron–hole pair's recombination · Dye degradation

S. Sridhar · A. Viswanathan (✉)
Department of Physics, Bharathidasan Institute of Technology (BIT) Campus, Anna University,
Tiruchirappalli 620 024, Tamilnadu, India
e-mail: alaganviswa@gmail.com

K. Venkateswarlu · N. Rameshbabu
Department of Metallurgical and Materials Engineering,
National Institute of Technology,
Tiruchirappalli 620 015, Tamilnadu, India

N. L. Parthasarathi
Materials Technology Division, Indira Gandhi Centre for Atomic Research, Kalpakkam 603 102, Tamilnadu, India
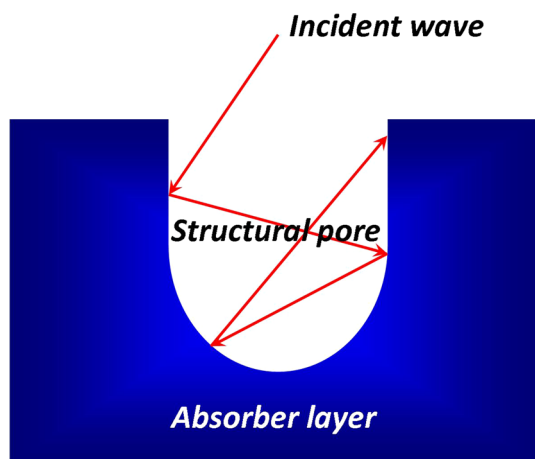
1 Introduction

Micro-arc oxidation is an advanced electrochemical oxidation method to produce porous ceramic coatings over transition metals (Ti, Al, Mg, Zr etc.,) and their alloys by rapid micro-arc discharges [1–4]. The micro-arc discharge takes place when an applied voltage exceeds the dielectric break down voltage of ceramic/oxide coatings [5]. MAO processed transition metals exhibits distinct properties like high productivity, high hardness, good wear resistance, excellent bonding strength with substrate and relatively low cost [6–9]. In addition, MAO provides substrate based oxides coatings with porous structure which may not be derived from any other conventional techniques. Hence, MAO covers wide range of applications in structural, functional and biomedical areas [6, 10]. Also, MAO is a suitable method for developing photocatalytic coatings as it can be produced a porous structured ceramic coating with favorable phase composition [11, 12]. A porous structured coating can increase the surface reactive areas which lead to higher photocatalytic activity. When light falls on the porous structured coatings, it undergoes multiple back and forth reflections consecutively which results part of the light energy absorbed during each contact (Fig. 1) [13]. The total absorptions will increase the photocatalytic

Fig. 1 Multiple absorption by back–forth reflections of light waves in the porous structured MAO coatings

activities by separation of more charge carriers. Thus, MAO based TiO$_2$ coatings have the tendency to increase the efficiency of absorption as well surface reactive area compared to the conventional TiO$_2$ particles and coatings.

Titanium dioxide is one of the most widely studied metal oxides for photocatalytic application due to its unique electronic and optical properties, high physical and chemical stability, low cost and nontoxicity [14, 15]. However, some drawbacks of TiO$_2$ such as wide band gap energy (3.2 eV) and high rate of electron–hole recombination restricts its range of practical applications only under UV irradiation ($\lambda < 388$ nm) [16, 17]. Therefore, many research works focused on TiO$_2$ to extend its optical absorption edge from UV to the visible-light region and to decrease the electron–hole recombination rate. The prominent way to encounter these limitations is to alter the band gap energy of TiO$_2$ via doping of some metals and non-metals [18–24].

Various methods have been followed to reduce the band gap energy of TiO$_2$ and thereby to improve the photocatalytic efficiency. Zhang et al. [19] prepared Ag cluster-doped TiO$_2$ nanoparticles by combined techniques of laser ablation in liquid and hydrothermal process. The band gap energy of Ag cluster-doped TiO$_2$ nanoparticles is found to be decreased to 3.06 eV. Ag/TiO$_2$ showed improved photocatalytic efficiency toward pentachlorophenol (PCP) degradation. Long et al. [20] prepared C$_{60}$-incorporated TiO$_2$ nano rods by hydrothermal process. They concluded that the enhanced photocatalytic activities under visible light maybe ascribed to an effective separation of the photoexcited electrons due to the addition of C$_{60}$. Asahi et al. [25] first reported that nitrogen doped into substitutional site of TiO$_2$ has proven to be indispensable for band gap narrowing and photocatalytic activity. Bayati et al. [26] developed $(WO_3)_X − (TiO_2)_{1−X}$ nano-structured porous

catalysts by micro arc oxidation and achieved band gap energy 2.87 eV. This coating showed better photo degradation on methylene blue (MB) dye under visible light.

From the existing literature, it could be noticed that the practical photocatalytic applications of the suspended TiO$_2$ system (in the form of colloidal and particulate) has the limitation to reuse. It is due to the difficulty in separating the TiO$_2$ particulates from water or pollutants and also the particles aggregation especially at higher concentration [27, 28]. To overcome these technical problems, various methods have been used to develop the immobilized TiO$_2$ photocatalytic coatings which can be reusable. However the photocatalytic efficiency of the immobilized coating system is much lower than the mobilized systems due to the reduction of overall surface reactive area.

Therefore, the present study made an attempt to develop porous structured coatings on commercially pure titanium (Cp-Ti) by MAO process. The coatings consist of C, N and F doping with TiO$_2$ to improve the surface reactive area and to reduce the band gap energy for visible light photocatalytic activities. Different electrolyte additives such as sodium carbonate (Na$_2$CO$_3$), sodium nitrate (NaNO$_2$) and potassium hexa fluoro titanate (K$_2$TiF$_6$) have been used to attain C, N and F doped TiO$_2$ coatings, respectively. The influence of chemical composition, surface morphology, surface amplitude parameters, phase composition, band gap energy variations, recombination rate of photogenerated electron–hole pairs and photocatalytic behaviour in MB dye of the coatings were investigated.

2 Materials and experimental methods

2.1 Materials

The Cp-Ti test plates with dimensions of 20 mm × 15 mm × 1.5 mm were cut from the plate and their surface were abraded up to 1000 grit emery paper. Then the specimens were ultrasonically cleaned in alcohol, acetone and distilled water solutions successively for about 5 min. Prior to MAO treatment the specimens were immersed in a diluted mixture of nitric and hydrofluoric acid for 30 s to remove the natural titanium oxide layer and surface contaminants.

2.2 Preparation of P-block element (C, N and F) doped TiO$_2$ coatings

Figure 2 shows the schematic diagram of the micro arc oxidation setup. The Cp-Ti plate was used as working electrode and the electrolyte container made of stainless steel used as the counter electrode. A DC power supply unit with a maximum peak voltage and current of 900 V and
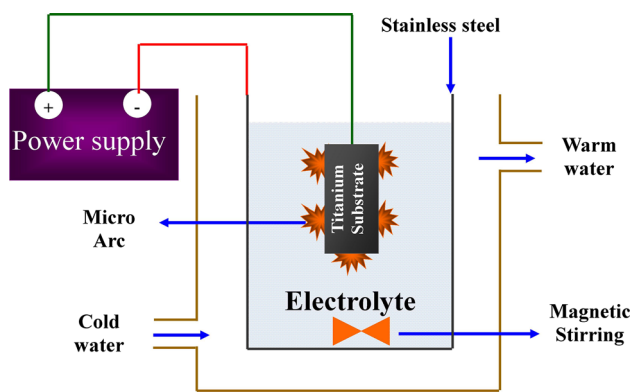
Fig. 2 Schematic setup of micro arc oxidation (MAO)

15 A respectively, was employed for MAO process. Aqueous electrolyte solutions consisting of sodium carbonate (Na_2CO_3), sodium nitrite ($NaNO_2$) and potassium hexa fluoro titanate (K_2TiF_6) with tri-sodium orthophosphate (TSOP, $Na_3PO_4 \cdot 12H_2O$) used as base electrolytes to develop $C\text{-}TiO_2$, $N\text{-}TiO_2$ and $F\text{-}TiO_2$ coatings on Cp-Ti respectively. The above said chemicals were purchased from Merck India Pvt. Ltd. All the experiments were carried out for 8 min at a constant current of 1 A. During the MAO process the electrolyte solution was stirred continuously to attain uniform distribution of electrolyte concentration and the electrolyte bath was maintained close to room temperature to control or avoid thermal activated growth process. The break down and final voltages were carefully noted and tabulated for all the coatings (Table 1). After MAO treatment, the samples were rinsed with distilled water and dried with hot air blower.

An aqueous tri-sodium orthophosphate (TSOP, $Na_3PO_4 \cdot 12H_2O$) solution was employed to develop pure TiO_2 coating on Cp-Ti under the same experimental conditions without dopant electrolyte for comparison with doped TiO_2.

2.3 Characterization of the MAO coatings

The phase composition of the prepared coatings was analyzed by Rigaku X-ray diffractometer (Ultima III, Rigaku, Japan) using Cu K_α radiation at 40 kV and 30 mA over 2θ range of $20°$–$80°$ with scan speed of $1°$/min and step size of 0.05°. The surface morphology, thickness and elemental composition of the coatings were studied using a Hitachi-S3000N scanning electron microscope (SEM) attached with energy dispersive spectroscopy (EDS) facility.

2.3.1 Surface profilometry

Surface amplitude parameters such as surface roughness, pores size and depth of the MAO samples were examined using optical Talysurf CLI 1000 surface profilometer. High resolution non-contact confocal point gauge was used for line profiling of MAO coatings. The resolution range of point gauge was 3000 μm with 0.25 nm. The focused beam through a lens with chromatic aberration was scanned on the surface of MAO coatings. Due to the aberration, the focus point was varied at different Z-position for different wavelengths. The reflected light from the porous coatings was allowed to fall on spectrometer through a pin hole. The spectrometer profile provides an intensity curve depending on wavelength. The focused wavelength was corresponding to the maximum intensity [29]. The surface profiles were analysed using Talymap Platinum software version 4.1.

2.3.2 Diffused reflectance UV–Vis spectrometer

UV–Vis diffuse reflectance spectrometer (carry 500) was used to measure the band gap energy of the MAO coatings in the wavelength range from 300 to 500 nm. From the reflectance spectra, the absorption was calculated based on the Kirchhoff's law $A(\lambda) + R(\lambda) + T(\lambda) = 1$ (where $A(\lambda)$, $R(\lambda)$ and $T(\lambda)$ are absorptance, reflectance and transmittance respectively) [5]. All the MAO coatings were completely opaque and hence their transmittance was assumed as zero. Thus, we have modified the Kirchhoff's law as $A(\lambda) = 1 - R(\lambda)$. Finally, the band gap energy (E_g) was calculated by standard method i.e. $E_g = hc/\lambda_m$ (where c is velocity of light in vacuum, h is Planck's constant and λ_m is cut-off wavelength obtained from absorption spectra). Photoluminescence experiments were conducted at room temperature by fluorescence spectrophotometer (FLUOROLOG—FL3-11) with Xenon lamp with an excitation wavelength of 300 nm.

2.3.3 Photocatalytic studies

Photocatalytic activity of pure and doped TiO_2 was evaluated by measuring the degradation rate of aqueous MB dye solution. A UV–Vis spectrophotometer was used to measure the rate of absorption based on the change in concentration of MB solution for every 30 min interval. The experiments were conducted in the 10 ml of MB solution with the concentration of 20 mg/L by immersing

Table 1 MAO processing parameters for TiO_2, $C\text{-}TiO_2$, $N\text{-}TiO_2$ and $F\text{-}TiO_2$

Coating	Electrolyte composition	V_b	V_f
TiO_2	5 g *TSOP*	350	460
$C\text{-}TiO_2$	5 g *TSOP* + 3 g Na_2CO_3	272	426
$N\text{-}TiO_2$	5 g *TSOP* + 3 g $NaNO_3$	278	429
$F\text{-}TiO_2$	5 g *TSOP* + 3 g K_2TiF_6	280	431

MAO produced photocatalyst. A Mercury lamp (250 W) was used as an irradiation light source which covers the wavelength ranging from 200 to 700 nm. However, the experiment was conducted along with UV cut off filter L-39 (Kenko co.) to limit the wavelength range below than 390 nm.

Prior to the experiment, the photocatalyst suspended solutions were kept in the dark condition for 60 min to attain adsorption–desorption equilibrium condition and then irradiated with mercury lamp.

In general, the adsorbed dye amount per unit mass of adsorbent (q_t) at any time are calculated based on the following equation [30]

$$q_t = \frac{C_0 - C_t}{m} \times V$$

where C_0 and C_t are the initial and variable time dye concentration (g/L) respectively, V is the solution volume (L) and m is the adsorbent mass (g). However, measuring the amount of photocatalyst mass (adsorbent mass) is difficult for MAO processed coatings. Hence, MAO produced photocatalyst were kept in dark atmosphere for 60 min (considered as reference point) [31] to attain adsorption–desorption equilibrium condition.

The absorptivity measurements were carried out at a fixed wavelength of 664 nm as MB solutions absorption was attained at this wavelength. The photocatalytic efficiency was calculated by $\eta = 1 - (C/C_o)0 \times 100$ % [32], where C_o and C are the initial and final (after irradiation) concentration of the MB solutions respectively.

3 Results and discussion

3.1 Surface morphology of MAO coating

Figure 3a–d shows the digital photograph of the MAO processed pure TiO_2, C-TiO_2, N-TiO_2, and F-TiO_2 coatings, respectively on Cp-Ti. The visual inspection of the
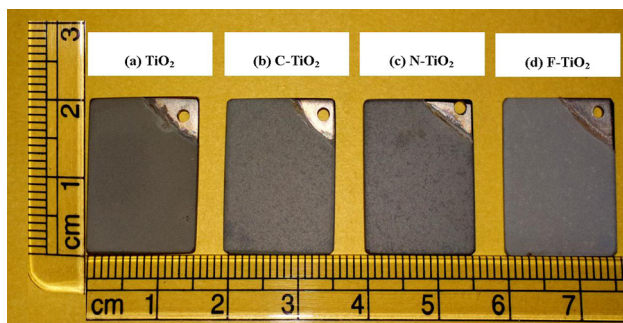

Fig. 3 Surface overview of TiO_2, C-TiO_2, N-TiO_2 and F-TiO_2 coatings

coatings reveals that the uniform coatings with crack free surfaces. The F-TiO_2 coating fabricated by the addition of K_2TiF_6 additive appears to be darker than the other coatings. Figure 4a–d shows the SEM surface morphology of pure TiO_2, C-TiO_2, N-TiO_2, and F-TiO_2 MAO coatings, respectively. The pure TiO_2 (Fig. 4a) coating shows different size and shape of the pores. The non-uniformly distributed pores varied in size from place to place and also they are not perfectly circular. The C-TiO_2 and N-TiO_2 (Fig. 4b, c) coatings exhibited not exactly like pores rather it consisted different configurations of narrow slits and oxide accumulations over the slits where dielectric break down occurs during MAO. Such surface morphology appearance depicted uniformly throughout the coatings. The F-TiO_2 coating (Fig. 4d) showed a canal like network structure with thicker crater walls. The significant surface morphological change from pure to doped TiO_2 is due to the discharge characteristics and conductivity nature of the electrolyte solution. Also, the formation of porous structures during MAO is due to dielectric breakdown occurring under applied potential exceeding the critical break down potential. However, any configuration of porous structure can enhance the surface reactive area which leads to improved photocatalytic activities.

Figure 5a–d shows the cross sectional view of pure TiO_2, C-TiO_2, N-TiO_2, and F-TiO_2 coatings on Cp-Ti. The coatings exhibited average thickness ranging from 18 to 26 μm. The variations of coating thickness can be attributed by MAO process parameters such as electrolyte conductivity, breakdown voltage and final voltage. All the MAO processed coatings showed good adherence with substrate. It is due to the formation of molten oxide layer and its subsequent solidification on the Cp-Ti during the MAO process.

3.2 Formation of porous structured coating by MAO

Figure 6 shows the schematic representation of series of action takes place during MAO process on Cp-Ti. Initially, the titanium surface gets oxidized in the appropriate electrolyte to form TiO_2 layer called as anodization. When an applied voltage exceeds the anodizing voltage [critical voltage (V_c)] micro-arcs are appeared on the TiO_2 coatings which is mentioned as dielectric breakdown. The effect of dielectric breakdown causes higher thermal energy which creates localized melting on TiO_2 coatings. Such thermal energy may sufficient to produce low and high temperature anatase and rutile phase of TiO_2 respectively [6]. The melted TiO_2 materials are ejected out and forms summits and valley over the anodized surface. The ejected melts are deposited on the outer surface of TiO_2 and consequently sintered to form dense and adherent ceramic layer on the surface. Finally the valley mostly consist titanium atoms
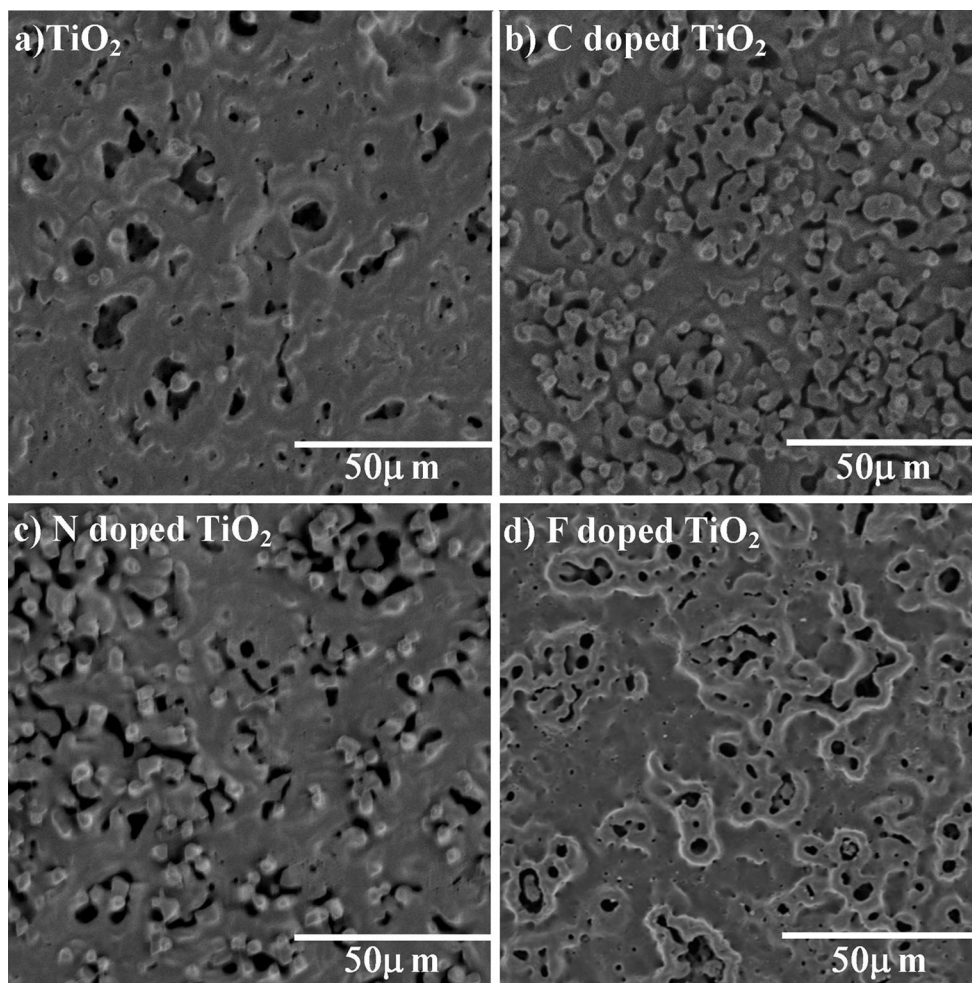
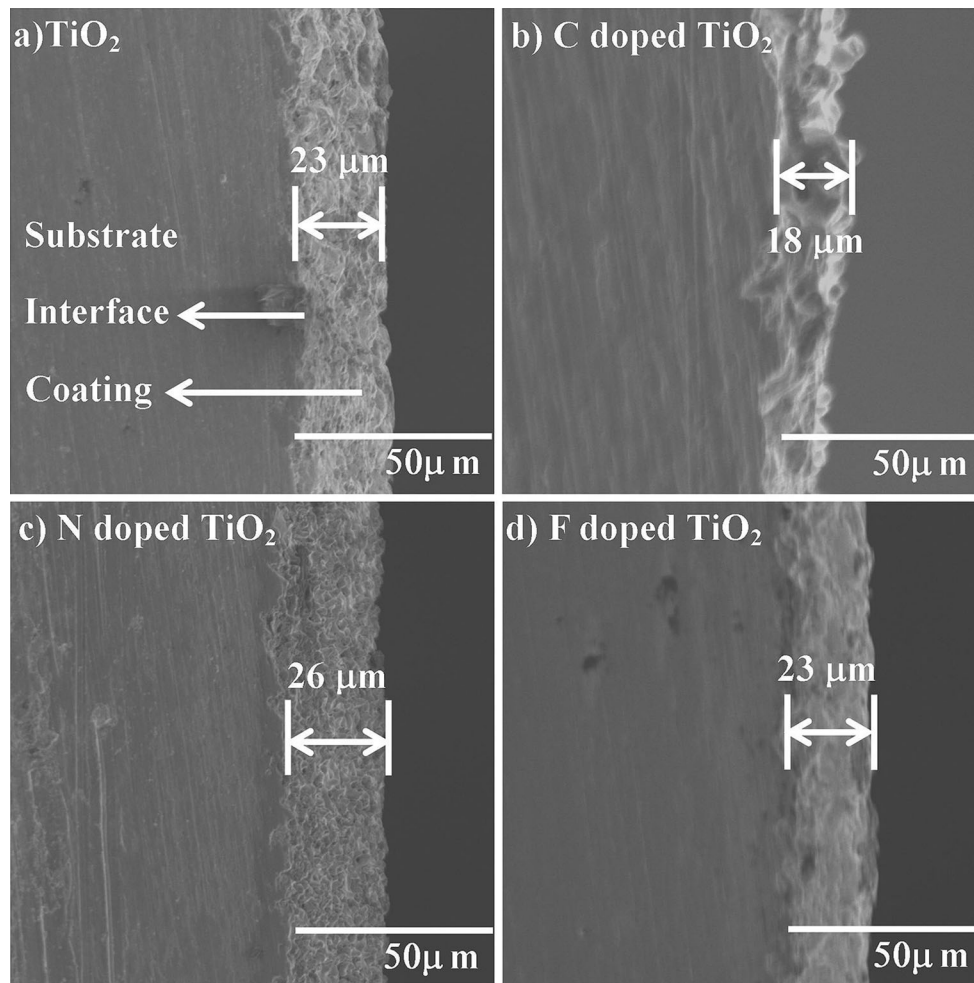**Fig. 4** SEM images of TiO_2, $C\text{-}TiO_2$, $N\text{-}TiO_2$ and $F\text{-}TiO_2$ surface morphology

than TiO_2 molecules gets oxidized by anodizing process again to form new TiO_2 layer. The MAO process continues until to form thick TiO_2 coating with high porosity. The pores depth and width of summits and valley depends on the amount of melt flow, nature of surface defects available on the surface of titanium, the electrolyte environment and micro-arc initiation time on that particular spot. Therefore, these parameters will vary to doping elements and surface condition of titanium surface.

3.3 Surface roughness analysis

Figures 7a–d and 8a–d show optical profile meter mesh images and line profiles for pure TiO_2, $C\text{-}TiO_2$, $N\text{-}TiO_2$ and $F\text{-}TiO_2$. The corresponding surface amplitude parameters are given in Table 2. Surface roughness increases in the order of $F\text{-}TiO_2 < C\text{-}TiO_2 < N\text{-}TiO_2 <$ pure TiO_2. The results clearly show that higher the break down (V_b) and final voltage (V_f) of the coatings lower the surface

roughness and vice versa (Fig. 9). The different electrolyte environment determines the different breakdown and final voltage of the MAO coatings. If the break down voltage is low, micro arcs (dielectric break downs) are initiated at the earlier stage which eventually results in higher porosity in the stipulated duration and vice versa. Even though pore depth of $F\text{-}TiO_2$ is higher than the other coatings, the roughness of $F\text{-}TiO_2$ is low. It is due to the low pores density as this was absorbed from the surface morphology analysis (SEM images) of the coatings.

The line profiles show higher crest and deeper troughs for $C\text{-}TiO_2$ and $N\text{-}TiO_2$ and lower crest and light troughs for $F\text{-}TiO_2$ and TiO_2, respectively. This indicates high amount of melt may come out during MAO process for $C\text{-}TiO_2$ and $N\text{-}TiO_2$. Whereas small amount of melt may comes out for $F\text{-}TiO_2$ and pure TiO_2. Figure 10 elaborates the variation of pores mean depth and width of pure and doped TiO_2 of MAO samples. The photocatalytic activity of MAO processed samples depends of all this surface amplitude parameters.

Fig. 5 Cross sectional view of TiO$_2$, C-TiO$_2$, N-TiO$_2$ and F-TiO$_2$ coatings

Fig. 6 MAO step by step process to produce porous coatings
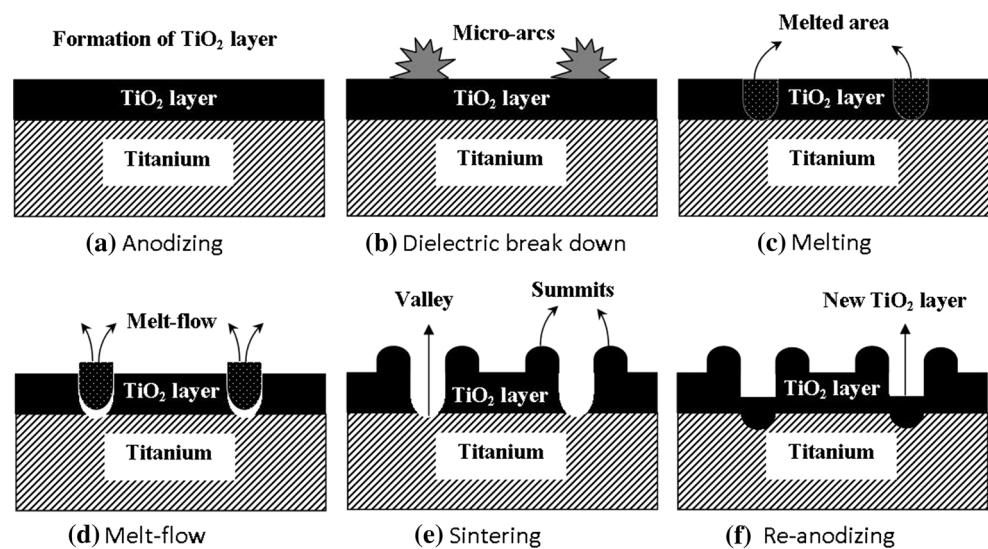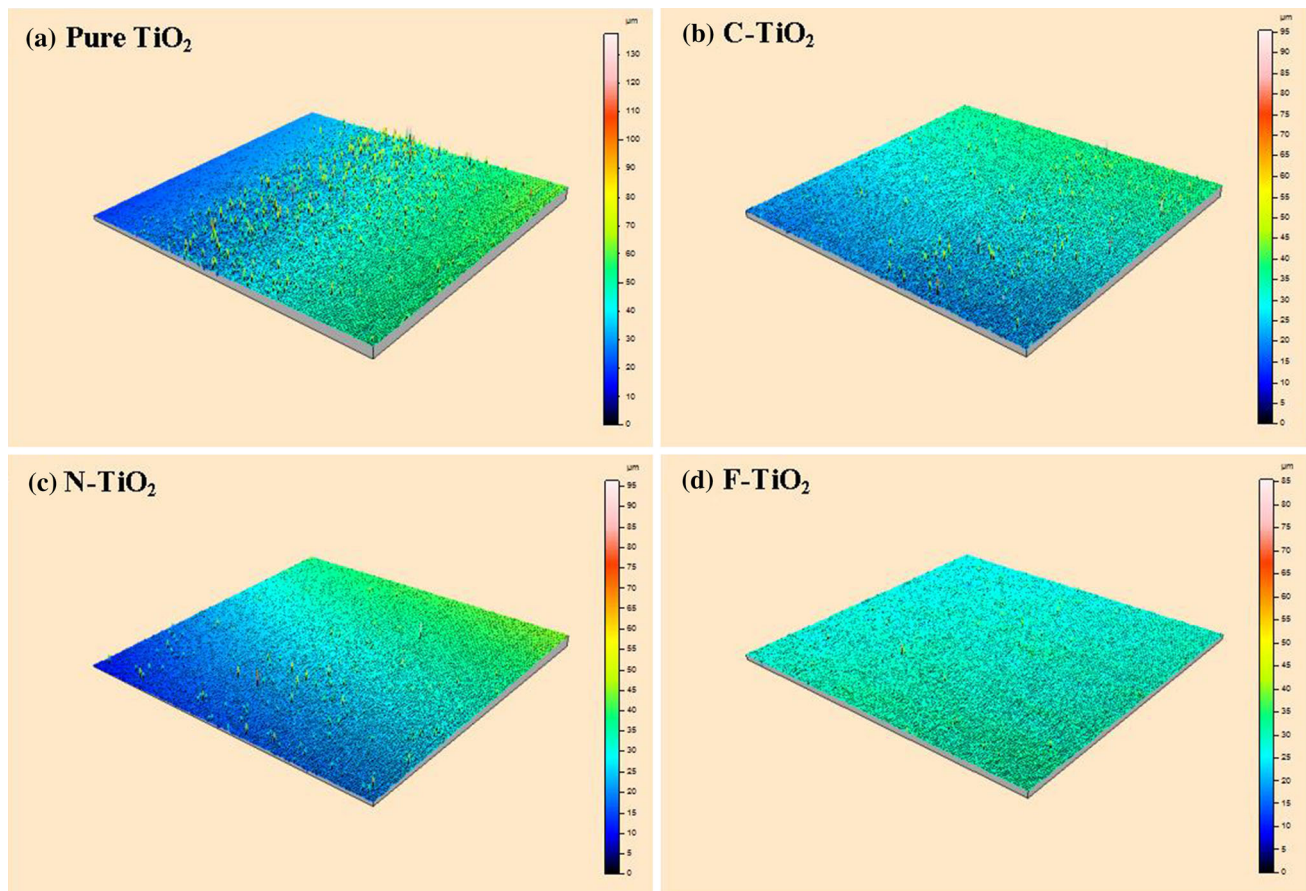
Fig. 7 Optical profilometer mesh images of TiO_2, $C-TiO_2$, $N-TiO_2$ and $F-TiO_2$ coatings

3.4 Phase and elemental analyses

Figure 11 shows the XRD patterns of MAO processed pure TiO_2 and C, N and F doped TiO_2 coatings on Cp-Ti substrate. Two prominent crystalline phases of TiO_2 (anatase and rutile) are existing in all the MAO coatings. In addition, the substrate (titanium) diffraction peaks also emerged along with the two oxide phases due to insufficient oxidation of titanium in the pores and small thickness of coatings [33]. The pure TiO_2 coating exhibited predominantly anatase phase with small percentage of rutile phase. Anatase and rutile phase percentage in the coatings is calculated by the following equations [6]

Anatase weight percent $(X_A) = I_A/(I_A + 1.26\ I_R)$

Rutile weight percent $(X_R) = I_R/(I_R + 0.8\ I_A)$

where X_R is rutile weight percent, I_A and I_R are the integrated diffraction peak intensities of anatase (101) and rutile (110) phases respectively. Using the above equation for the estimation of phases, it is found that the amount of anatase to rutile phase ratio decreased in the order of $TiO_2 > C-TiO_2 > F-TiO_2 > N-TiO_2$ coatings with reference to the

relative intensity of characteristic peaks (Table 3). In general, the MAO process would initiate the oxide layer on Cp-Ti in the form of amorphous and metastable crystalline anatase phase of TiO_2. At the later stages of MAO process, the micro-arc generates higher local temperature which may promote the transformation of amorphous and metastable anatase phase into high temperature rutile phase [11]. Based on the electrolyte chemistry the discharge characteristics differ and determines the amount of anatase to rutile phase transformation.

Absence of C, N and F phases from the XRD pattern, the EDS analysis was carried out to confirm the doped elements in the coatings. Figure 12a–d shows the EDS spectra and mapping of elements on the surface of pure TiO_2 and C, N and F doped TiO_2 coatings respectively. In addition to Ti and O elements, phosphorous also present in the coatings due to the use of Na_3PO_4 electrolyte during MAO process. Spectrum quantification has been also carried out from EDS results for MAO processed coatings and presented in the Table 4. The elemental mapping and EDS analyses confirmed the presence of 2.2 at.% C, 3.1 at.% N and 3.8 at.% F
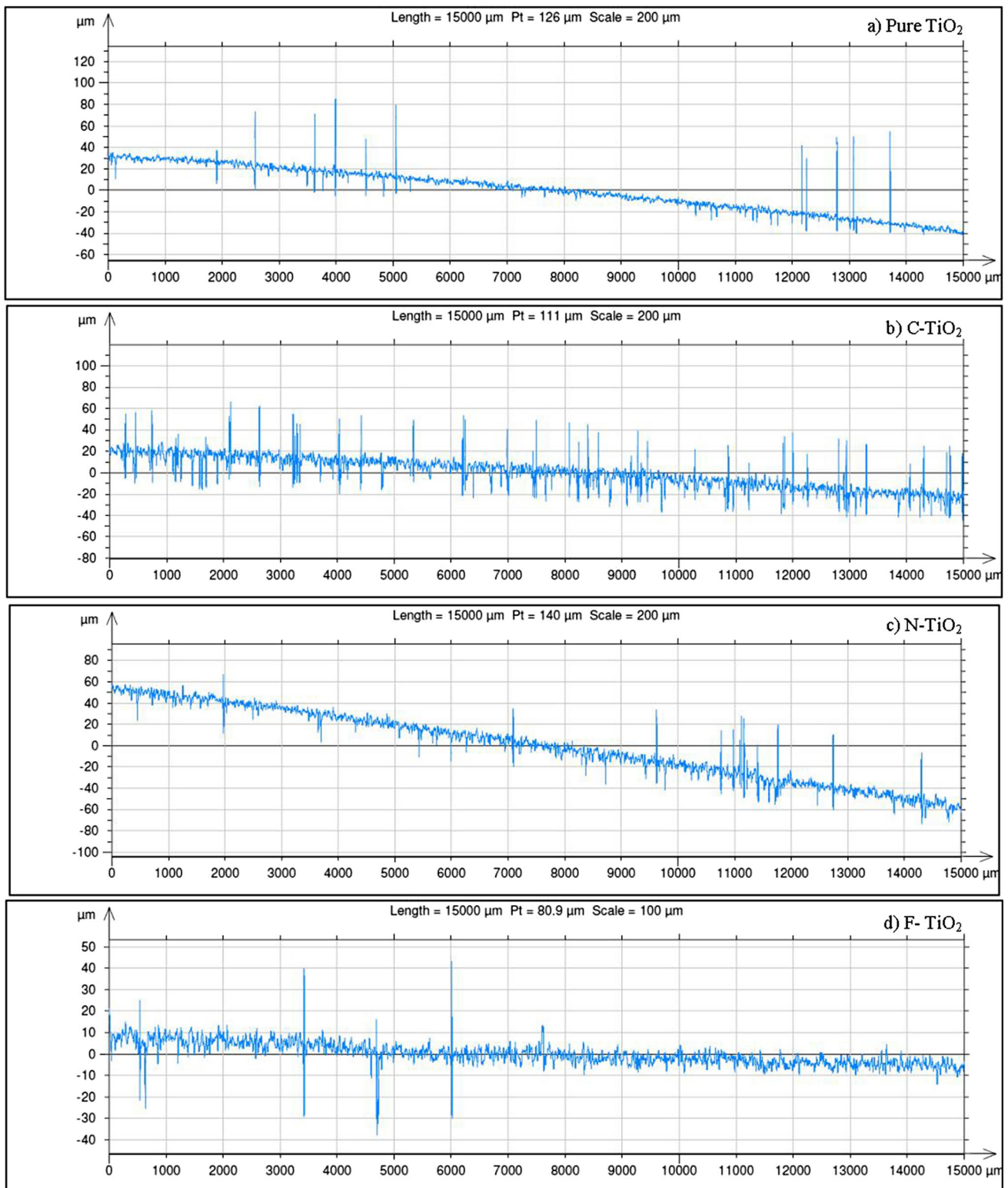
Fig. 8 Optical profilometer line profile of TiO$_2$, C-TiO$_2$, N-TiO$_2$ and F-TiO$_2$ coatings

Table 2 Surface amplitude parameters for TiO₂, C-TiO₂, N-TiO₂ and F-TiO₂

| Coatings	R_a	R_q	R_p	R_v	R_t	R_{sk}	R_{ku}	R_z
Pure TiO₂	1.63	3.27	27	11.8	104	16	320	38.8
C-TiO₂	3.91	6.45	40.8	25.3	81.1	0.909	15.3	66.2
N-TiO₂	2.74	4.28	21.2	20.6	80.5	21.6	37.1	41.8
F-TiO₂	1.99	1.95	9.6	6.86	75.6	11.1	331	16.5

R_a, Arithmetic mean deviation of the roughness profile; R_q, Root-mean-square deviation of the roughness profile; R_p, Maximum peak deviation of the roughness profile; R_v, Maximum valley depth of the roughness profile; R_t, Total height of the roughness profile; R_{sk}, Skewness of the roughness profile; R_{ku}, Kurtosis of the roughness profile; R_z, Maximum height of the roughness profile
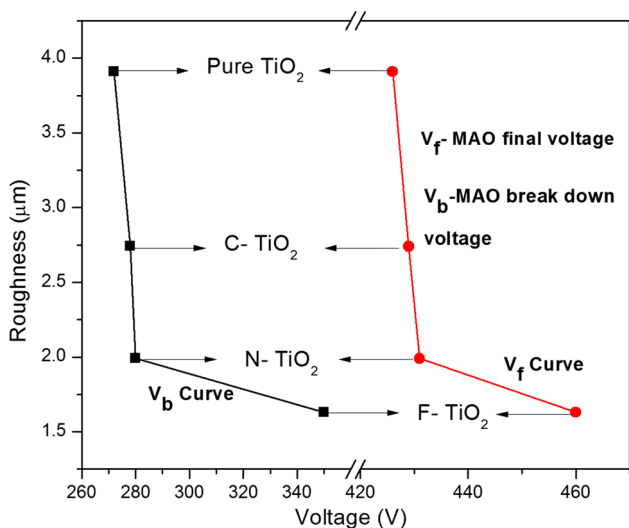
Fig. 9 Voltage versus roughness of TiO₂, C-TiO₂, N-TiO₂ and F-TiO₂ coatings
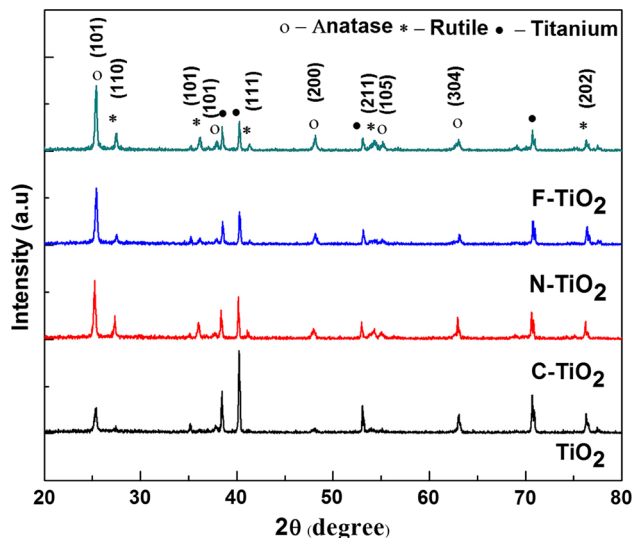
Fig. 11 XRD patterns of TiO₂, C-TiO₂, N-TiO₂ and F-TiO₂ coatings
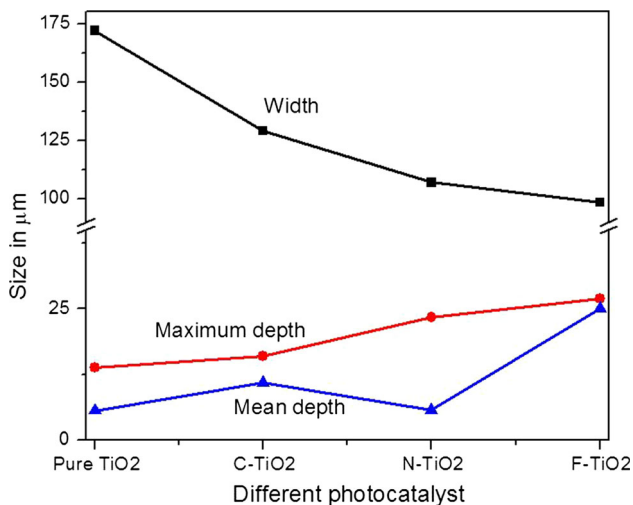
Fig. 10 Pore depth and width comparison of TiO₂, C-TiO₂, N-TiO₂ and F-TiO₂ coatings

Table 3 Anatase and rutile phase percentage in TiO₂, C-TiO₂, N-TiO₂ and F-TiO₂

Coating	Anatase (%)	Rutile (%)
TiO₂	66.86	33.14
C doped TiO₂	67.38	32.62
N doped TiO₂	82.93	17.07
F doped TiO₂	76.73	23.27

3.5 UV–Vis diffuse reflectance spectroscopy (DRS) analysis

Figure 13 shows the UV–Vis diffuse reflectance spectra of pure and doped TiO₂ coatings. From the spectra, the absorption edges of pure TiO₂ and C, N and F doped TiO₂ were obtained at 393, 409, 407 and 410 nm respectively and their corresponding band gap energies were calculated as 3.15, 3.03, 3.04 and 3.02 eV. Also, the UV–Vis absorption spectra show the enhanced absorption for pure
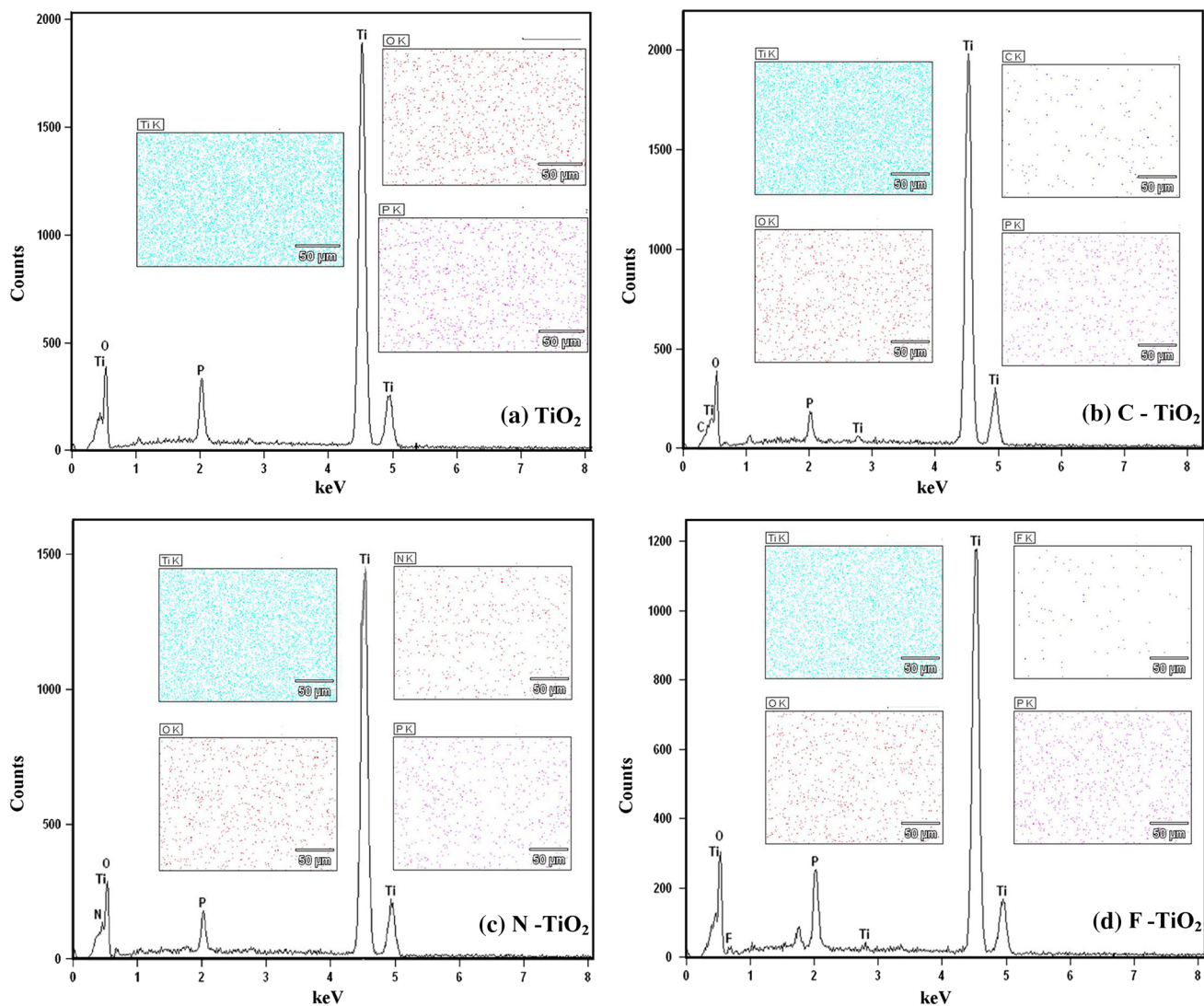
elements in the coatings. In addition the elemental mapping exhibited uniform distribution of doped elements in the coatings.

Fig. 12 a–d EDS spectrum and dot mapping of pure TiO_2, $C-TiO_2$, $N-TiO_2$ and $F-TiO_2$ coatings

Table 4 Elemental compositions of TiO_2, $C-TiO_2$, $N-TiO_2$ and $F-TiO_2$

| Coating	Ti (at.%)	O (at.%)	P (at.%)	C (at.%)	N (at.%)	F (at.%)
Pure TiO_2	43.4	52.7	3.9	–	–	–
$C-TiO_2$	44.7	51.1	1.9	2.2	–	–
$N-TiO_2$	37.6	57.3	2.0	–	3.1	–
$F-TiO_2$	34.8	54.4	4.2	–	–	3.8

TiO_2 than doped TiO_2 even the cut off wave length of pure TiO_2 is lower than that of doped TiO_2 samples. The enhanced absorption of pure TiO_2 may attributed by higher pores concentration and its phase structure [31]. As evidenced by Figs. 9 and 10, the pore width and surface roughness of pure TiO_2 sample is higher than the doped TiO_2. The large pores width of pure TiO_2 may have multiple back and forth reflections which may enhanced the absorption compared to doped TiO_2.

Further, the calculated band gap energy of MAO processed pure TiO_2 (3.15 eV) exhibited lower than that of the normal TiO_2 (3.2 eV) which may be due to the presence of phosphorous in TiO_2 coatings as observed from the EDS spectra. However, the band gap energy of C, N, F doped TiO_2 coatings are considerably narrowed as compared to pure TiO_2 coating. The band structure of TiO_2 consists of a valence band and conduction band made primarily by O $2p$ and Ti $3d$ orbital's, respectively. The valance band
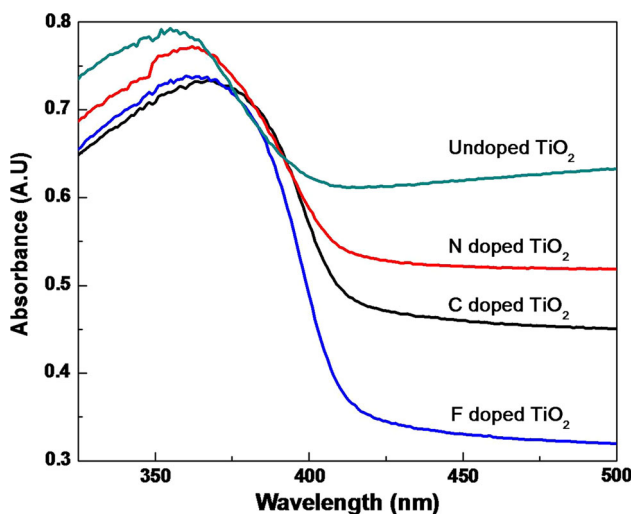
Fig. 13 UV–Vis diffuse reflectance spectra of TiO$_2$, C-TiO$_2$, N-TiO$_2$ and F-TiO$_2$ coatings

orbital of nitrogen (2P) and carbon (2P) mixes with the valance orbital (2P) of TiO$_2$ and lifts up the valance band of TiO$_2$ which results in the band gap energy reduction of TiO$_2$ (Fig. 14) [34]. In the aspect of F doping, the literatures claim that the 2p states of F appear below the valence band of TiO$_2$ and hence it cannot contribute much for band gap energy reduction of TiO$_2$ [35]. However, in contradictory with above results, we obtained reduced band gap energy of 3.02 eV when TiO$_2$ doped with F. In general, the band gap energy of rutile phase is lower than that of anatase phase TiO$_2$ and doping of phosphorous into TiO$_2$ may resulted in the band gap energy reduction. Therefore the influence of higher quantity of rutile phase and phosphorous element (4.2 at.%) in F doped TiO$_2$ coatings might play important role in the band gap energy reduction. Hence narrow downing the band-gap energy of TiO$_2$ can facilitate easy excitation of electrons from the valance band to the conduction band which will enhance the photocatalytic activities in the visible region [36].
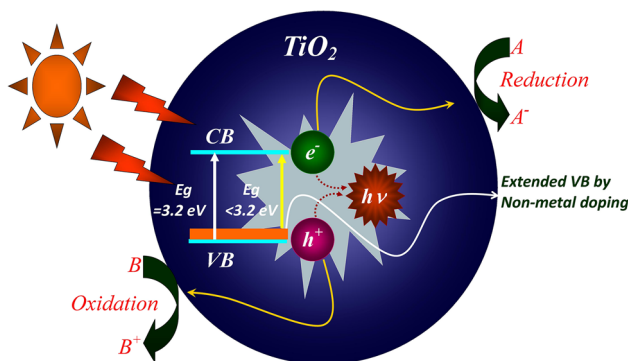
Fig. 14 Schematic illustration of band gap energy reduction of TiO$_2$ with dopants
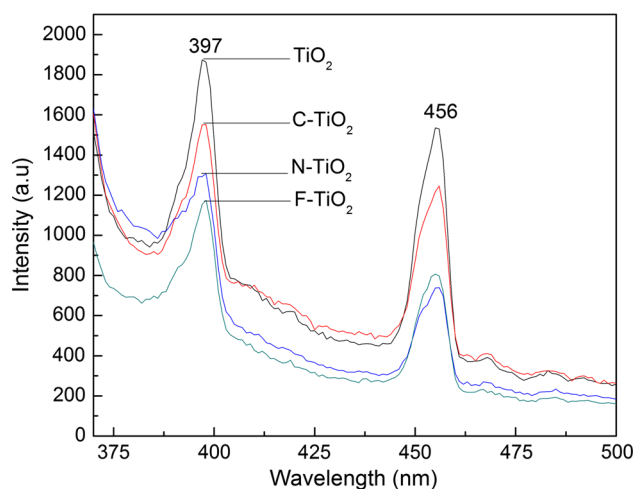
Fig. 15 PL spectra of pure and doped TiO$_2$

3.6 PL analysis of pure and doped TiO$_2$

Figure 15 shows the PL spectra of the pure and C, N and F doped TiO$_2$ coatings for an excitation wavelength of 300 nm. The spectra of pure and doped TiO$_2$ were almost similar except peak intensity variation. Two major emissive peaks were obtained in the scanning wavelength range of 370–500 nm. The first peak at 397 nm emerged by free exciton and second peak at 456 nm due to bound exciton. Generally, the free exciton emission occurred by the recombination of an excited electron in the conduction band with a hole in the valence band. The bound exciton emission is due to defect state electron–hole recombination which emits lower energy (red shift) than the free exciton [37]. The intensity of the PL spectra decreases in the order of TiO$_2$ > C-TiO$_2$ > N-TiO$_2$ > F-TiO$_2$ which indicates the change of electron–hole recombination rate with respect to dopant. It is well known that the lower PL intensity indicating lower the recombination rate of photogenerated electron–hole pairs, which favours for the enhanced photocatalytic activity. Therefore, the PL result proved that the doped TiO$_2$ offers lower recombination rate than the pure TiO$_2$. In particular, the luminescence intensity of F doped was lower than that of other doped TiO$_2$ samples which leads to enhanced photocatalytic activity.

3.7 Photocatalytic activity of pure and doped TiO$_2$ coatings

To investigate the photocatalytic activity of pure and doped TiO$_2$ coatings, MB dye was used as a model pollutant under the mercury vapor lamp irradiation. Figure 16 shows the photocatalytic efficiency of pure and doped TiO$_2$ coatings with respect to irradiation time. It was found that the efficiency of photodegradation increases with
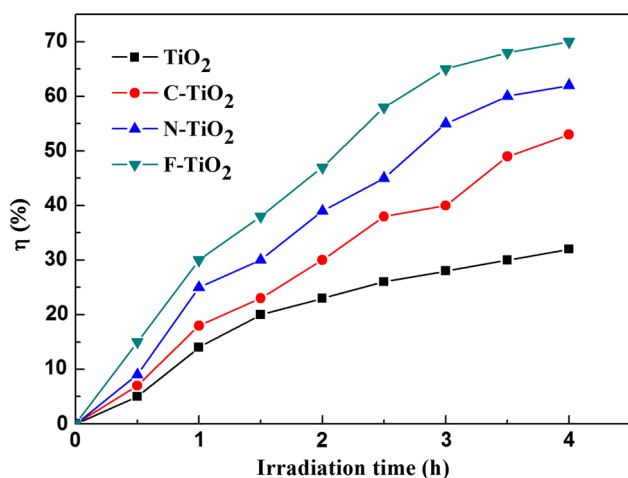
Fig. 16 Photocatalytic efficiency versus irradiation time

increasing of irradiation time. However, the percentage of MB dye degradation varied based on the dopant of TiO_2. For instance, 50 % of MB dye degradation takes place at 2.4, 2.78, 3.29 and 4 h for $F-TiO_2$, $N-TiO_2$, $C-TiO_2$ and TiO_2 coatings respectively. The photocatalytic efficiency of the coatings varies in the order of $F-TiO_2 > N-TiO_2 > C-TiO_2 > TiO_2$ as it was expected from the results of PL and UV–Vis spectroscopy analyses. Though the rate of absorption of pure TiO_2 was higher than that of doped TiO_2 (Fig. 13), the rate of MB dye degradation shown better result for $F-TiO_2$ coating. It may be attributed due to the reduced band gap energy as well appropriate percentage of anatase and rutile phase structure [31]. Hence, it was confirmed from the obtained results, the photocatalytic efficiency was increased when the rate of photogenerated electron–hole pair's recombination was decreased.

4 Conclusions

1. A new type of immobilized, porous and visible light active P-block elements (C, N and F) doped TiO_2 coatings were developed by micro arc oxidation technique.

2. MAO produced porous coatings increased the surface reactive area which enhanced the photocatalytic activity. Surface roughness increases in the order of $F-TiO_2 < C-TiO_2 < N-TiO_2 < pure\ T_iO_2$.

3. The obtained band gap energies were 3.03, 3.04 and 3.02 for C, N and F doped TiO_2 coatings respectively, whereas for pure TiO_2 coating was exhibited 3.15 eV. The reduced band gap energy and appropriate percentage of anatase and rutile phase structure of doped TiO_2 samples resulted in higher photocatalytic activity under visible light.

4. The photogenerated electron–hole pair's recombination rate was effectively inhibited by doping of C, N and F into TiO_2 which attributes enhanced photocatalytic efficiency.

5. Doped TiO_2 showed enhanced photocatalytic activity with MB dye compared to pure TiO_2. Particularly, $F-TiO_2$ revealed maximum photocatalytic activity among all other doped TiO_2.

References

1. D. Sreekanth, N. Rameshbabu, Mater. Lett. **68**, 439 (2012)
2. S.P. Sah, Y. Tatsuno, Y. Aoki, H. Habazaki, Corros. Sci. **53**, 1838 (2011)
3. Y. Wang, Z. Jiang, Z. Yao, Appl. Surf. Sci. **256**, 650 (2009)
4. W. Shang, B. Chen, X. Shi, Y. Chen, X. Xiao, J. Alloys Compd. **474**, 541 (2009)
5. M.R. Bayati, F. Golestani-Fard, A.Z. Moshfegh, Catal. Lett. **134**, 162 (2010)
6. K. Venkateswarlu, N. Rameshbabu, D. Sreekanth, A.C. Bose, V. Muthupandi, S. Subramanian, Ceram. Int. **39**, 801 (2013)
7. L. Rama Krishna, K.R.C. Somaraju, G. Sundararajan, Surf. Coat. Technol. **163–164**, 484 (2003)
8. D. Sreekanth, N. Rameshbabu, K. Venkateswarlu, Ceram. Int. **38**, 4607 (2012)
9. C.S. Dunleavy, I.O. Golosnoy, J.A. Curran, T.W. Clyne, Surf. Coat. Technol. **203**, 3410 (2009)
10. J.A. Curran, T.W. Clyne, Acta Mater. **54**, 1985 (2006)
11. K.R. Wu, C.H. Hung, C.W. Yeh, J.K. Wu, Appl. Surf. Sci. **263**, 688 (2012)
12. M.R. Bayati, A.Z. Moshfegh, F. Golestani-Fard, Appl. Surf. Sci. **256**, 2903 (2010)
13. M.R. Bayati, H.R. Zargar, A. Talimian, A. Ziaee, R. Molaei, Surf. Coat. Technol. **205**, 2483 (2010)
14. E.M. Neville, M.J. Mattle, D. Loughrey, B. Rajesh, M. Rahman, J.M.D. Mac Elroy, J.A. Sullivan, K.R. Thampi, J. Phys. Chem. C **116**, 16511 (2012)
15. H. Ozaki, S. Iwamoto, M. Inoue, J. Phys. Chem. C **111**, 17061 (2007)
16. H. Liu, Y. Wu, J. Zhang, ACS Appl. Mater. Interfaces **3**, 1757 (2011)
17. Y. Xu, Y. Zhuang, X. Fu, J. Phys. Chem. C **114**, 2669 (2010)
18. X. Lin, F. Rong, X. Ji, D. Fu, Microporous Mesoporous Mater. **142**, 276 (2011)
19. H. Zhang, C. Ling, J. Liu, Z. Tian, G. Wang, W. Cai, Langmuir **28**, 3938 (2012)
20. Y. Long, Y. Lu, Y. Huang, Y. Peng, Y. Lu, S. Kang, J. Mu, Effect of C_{60} on the photocatalytic activity of TiO_2 nano rods. J. Phys. Chem. C **113**, 13899 (2009)
21. J. García-Serrano, E. Gómez-Hernández, M. Ocampo-Fernández, U. Pal, Curr. Appl. Phys. **9**, 1097 (2009)
22. Y. Liu, J.H. Wei, R. Xiong, C.X. Pan, J. Shi, Appl. Surf. Sci. **257**, 8121 (2011)
23. D. Wu, M. Long, W. Cai, C. Chen, Y. Wu, J. Alloys Compd. **502**, 289 (2010)
24. C. Han, M. Pelaez, V. Likodimos, A.G. Kontos, P. Falaras, K. O'Sheac, D.D. Dionysiou, Appl. Catal. B Environ. **107**, 77 (2011)
25. R. Asahi, T. Morikawa, T. Ohwaki, K. Aoki, Y. Taga, Science **293**, 269 (2001)

26. M.R. Bayati, A.Z. Moshfegh, F. Golestani-Fard, R. Molaei, Mater. Chem. Phys. **124**, 203 (2010)
27. C. Wang, M. Wang, K. Xie, Q. Wu, L. Sun, Z. Lin, C. Lin, Nanotechnology **22**, 305607 (2011)
28. Y. Hong, D. Li, J. Zheng, G. Zou, Nanotechnology **17**, 1986 (2006)
29. H. Sun, H. Liu, J. Ma, X. Wang, B. Wang, L. Han, J. Hazard Mater. **156**, 552 (2008)
30. S. Jafari, S. Azizian, B. Jaleh, Colloid Surf. A **384**, 618 (2011)
31. M.R. Bayati, F. Golestani-Fard, A.Z. Moshfegh, R. Molaei, Mater. Chem. Phys. **128**, 427 (2011)
32. C.W. Dunnill, A. Kafizas, I.P. Parkin, Chem. Vap. Depos. **18**, 89 (2012)
33. N.L. Parthasarathi, U. Borah, S.K. Albert, Mater. Des. **51**, 678 (2013)
34. M.V. Dozzi, E. Selli, J. Photochem. Photobiol. C Photochem. Rev **14**, 13 (2013)
35. Z. Yao, F. Jia, S. Tian, C. Xiang, Z. Jiang, X. Bai, Appl. Mater. Interfaces **2**, 2617 (2010)
36. G. Halasi, I. Ugrai, F. Solymosi, J. Catal. **281**, 309 (2011)
37. A. Kitai, *Luminescent materials and applications* (Wiley, London, 2008)